JOURNAL OF APPLIED CRYSTALLOGRAPHY

ISSN: 1600-5767

journals.iucr.org/j

Microstrain distributions in polycrystalline thin films measured by X-ray microdiffraction

N. Schäfer, G. A. Chahine, A. J. Wilkinson, T. Schmid, T. Rissom, T. U. Schülli and D. Abou-Ras

J. Appl. Cryst. (2016). **49**, 632–635

JOURNAL OF APPLIED CRYSTALLOGRAPHY

ISSN 1600-5767

Received 14 September 2015
Accepted 24 February 2016

Edited by G. Renaud, CEA-Grenoble DSM/INAC/SP2M/NRS, Grenoble, France

Keywords: microstrain distribution; X-ray microdiffraction; polycrystalline thin films.

Microstrain distributions in polycrystalline thin films measured by X-ray microdiffraction

N. Schäfer,[a]* G. A. Chahine,[b] A. J. Wilkinson,[c] T. Schmid,[d] T. Rissom,[a] T. U. Schülli[b] and D. Abou-Ras[a]

[a]Helmholtz Zentrum Berlin für Materialien und Energie GmbH, Hahn-Meitner-Platz 1, Berlin 14109, Germany, [b]European Synchroton Radiation Facility, Grenoble Cedex, BP 220, France, [c]Department of Materials, University of Oxford, Parks Road, Oxford OX1 3PH, UK, and [d]Federal Institute for Materials Research and Testing, Richard-Willstätter-Strasse 11, Berlin 12205, Germany. *Correspondence e-mail: norbert.schaefer@helmholtz-berlin.de

Microstrain distributions were acquired in functional thin films by high-resolution X-ray microdiffraction measurements, using polycrystalline $CuInSe_2$ thin films as a model system. This technique not only provides spatial resolutions at the submicrometre scale but also allows for analysis of thin films buried within a complete solar-cell stack. The microstrain values within individual $CuInSe_2$ grains were determined to be of the order of 10^{-4}. These values confirmed corresponding microstrain distribution maps obtained on the same $CuInSe_2$ layer by electron backscatter diffraction and Raman microspectroscopy.

Strain in functional thin films can be correlated to the presence of extended structural defects such as dislocations and grain boundaries, which affect the performance of an optoelectronic device composed of a thin-film stack (Sun *et al.*, 2007). With respect to polycrystalline thin films exhibiting average grain sizes of below 1 µm, the method of analyzing strain needs to provide a corresponding spatial resolution.

High-resolution X-ray microdiffraction (µ-HRXRD) applied at a specialized synchrotron beamline not only fulfills this prerequisite but also enables one to study elastic microstrain in a thin film buried within a layer stack by measuring one-dimensional interplanar distance variations. As a model system, polycrystalline $CuInSe_2$ thin films used as absorber layers for solar cells were chosen. These thin films exhibit average grain sizes of about 1 µm. In addition to µ-HRXRD, further microstrain measurements were performed by means of electron backscatter diffraction (EBSD) and Raman microspectroscopy on $CuInSe_2$ thin films of the same deposition run for comparison.

The $CuInSe_2$ thin films were deposited on Mo-coated glass substrates by three-stage co-evaporation (Kaufmann *et al.*, 2005; Caballero *et al.*, 2013). Solar cells were completed by the deposition of a CdS buffer layer and an i-ZnO/n-ZnO:Al bilayer as window layer on top. Homogeneous distributions of the elements in the $CuInSe_2$ layer were confirmed by energy-dispersive X-ray spectroscopy conducted in a scanning electron microscope as well as by glow-discharge optical emission spectroscopy. Microstrain distribution maps were acquired by Raman microspectroscopy and EBSD performed on the surfaces of $CuInSe_2$/Mo/glass stacks prepared by etching away the ZnO:Al/i-ZnO/CdS layers using low-concentration HCl. In order to reduce surface roughness for EBSD measurements, a bromide-etching step was performed, and the surface quality of the samples was further improved by a final

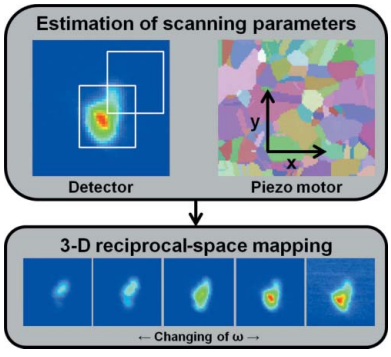

polishing step using a colloidal silica suspension (OPS by Struers). A nominally 5 nm-thick carbon layer was deposited on the examined surface to reduce charging during the EBSD investigation.

Raman spectra were collected using a LabRam HR 800 instrument (Horiba Jobin Yvon, Bensheim, Germany) coupled to a BX41 microscope (Olympus, Hamburg, Germany). An HeNe laser having a wavelength of 632.8 nm and a power of approximately 1 mW at the sample was used for excitation. The $CuInSe_2$ samples were investigated using a 100×/N.A. = 0.9 objective for both excitation and collection. Spectra were acquired by dispersing the collected light with a grating having 1800 grooves per millimetre and using a 1024 × 256 pixel CCD detector (Symphony, Horiba Jobin Yvon, liquid-N_2 cooled, 147 K operating temperature). With this configuration the spectral resolution is approximately 0.3 cm^{-1} per CCD pixel at the position of the most prominent (A_1) mode of the $CuInSe_2$ spectrum (Schmid *et al.*, 2015). For strain evaluation, the peak position of the A_1 mode was fitted using a Gaussian function which led to an actual spectral resolution of approximately 0.05 cm^{-1} (Becker *et al.*, 2007). Data processing was performed using custom-written *LabVIEW*-based software (Schmid *et al.*, 2015). For the determination of band shifts, an unstrained position was defined by averaging over the measured wavenumbers within the investigated grain. Individual grains were resolved on the basis of orientation-distribution maps composed of changing Raman intensities (Schmid *et al.*, 2015). The pressure dependence of the A_1 mode peak position described in the literature (González *et al.*, 1992; Theodoropoulou *et al.*, 2009) was used to convert wavenumber positions of the Gauss peaks into stress values (in GPa). To overcome the influence of the spectrometer calibration, only the slope of the pressure dependence of the A_1 mode was used, leading to a linear relation between actual wavenumber shifts and stress values of 5 cm^{-1} GPa^{-1}. Microstrain values were determined by using a value of Young's modulus of 68.8 GPa for $CuInSe_2$ (Berger, 1996).

The EBSD measurements were conducted using a Zeiss Ultraplus scanning electron microscope equipped with an Oxford Instruments NordlysNano camera. An accelerating voltage of 15 kV and beam currents up to 55 nA were used with a step size of 50 nm and no hardware binning to achieve best pattern quality. The cross-correlation analysis (also sometimes called high-resolution EBSD) (Wilkinson *et al.*, 2006) was performed on patterns at a resolution of 1344 × 1024 pixels, using 50 regions of interest (ROI) circularly arranged around the pattern, each exhibiting a resolution of 256 × 256 pixels. The reference pattern was selected on the basis of pattern quality and the position of the grain boundaries. The reference pattern defines the unstrained position within the grain, and shifts between the reference and other patterns are used to assess microstrain changes (Wilkinson, 1996). Out-of-plane microstrain distributions were calculated by assuming that the free surface of the sample was traction free (Dingley *et al.*, 2010). The extracted microstrain values were restricted concerning sensitivity and possible failure of the method (Wilkinson *et al.*, 2006). For the display of the results, an average weighted distribution was plotted for the out-of-plane values.

All μ-HRXRD measurements were performed at the ID01 beamline at the European Synchrotron Radiation Facility, Grenoble, France, using a monochromatic X-ray beam at an X-ray energy of 8.9 keV with an energy resolution of $\delta E/E = 10^{-4}$ resulting from an Si(111) double reflection monochromator. The beam was focused by a Fresnel zone plate, and the beam size at the sample position was about 100 × 100 nm. With this setup, μ-HRXRD provides access to microstrain and tilt variations with sensitivities of 10^{-5} ($\Delta a/a$) and 10^{-3}° (Chahine *et al.*, 2014, 2015), while the resolution of μ-HRXRD is mainly limited by two parameters. The beam size defines the real-space resolution and the beam divergence the resolution in reciprocal space. Their relation is described by the classical diffraction limit.

Fig. 1 shows a schematic drawing of the experimental setup used at the ID01 beamline. A variation of strain in the sample affects the scattering angle 2Θ at which the diffraction peak is found, as well as the rocking angle ω (angle of incidence in the meridional plane). A variation of lattice orientation (referred to as tilt) in the meridional plane would only lead to a variation of ω at unchanged 2Θ value. In a similar manner, tilt variations in the sagittal direction lead to an angular displacement ν in the sagittal direction of the reflected beam. Strictly speaking, this displacement happens along a Debye–Scherrer ring without impact on the value of the total scattering angle 2Θ. In order to determine the orientation and the strain in the lattice, the angles ω, 2Θ and ν are necessary for the complete description of the scattering vector **Q**. Using a two-dimensional detector and varying the angle of incidence ω, for each ω value each detector pixel is converted into detector angles,

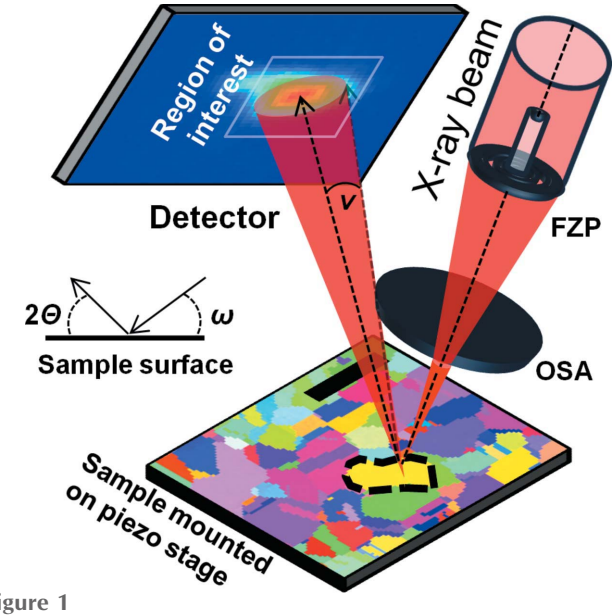

Figure 1
Schematics of the experimental setup for high-resolution microdiffraction, showing an X-ray beam impinging on a polycrystalline $CuInSe_2$ layer, and the diffracted beam hitting the detector. FZP = tungsten Fresnel zone plate. OSA = order sorting aperture (50 μm molybdenum).

and their reciprocal coordinates lead to a reciprocal three-dimensional peak for every real-space position (Chahine *et al.*, 2014). The conversion of the detector data into reciprocal space was done using the *xrayutilities* software (Kriegner *et al.*, 2013). One-dimensional Gaussian peak fitting is performed. The idea is to sum in two dimensions and to perform the fitting on a curve. This is repeated for all three dimensions using the least-squares fitting to locate the precise Q_x, Q_y and Q_z. The fit routine was performed using the *X-SOCS* software package (https://sourceforge.net/projects/xsocs/).

The experimental approach for mapping of individual $CuInSe_2$ grains is graphically summarized in Fig. 2. Firstly, by estimation of the appropriate incidence angles for the selected *hkl* reflections, atomic planes fulfilling the diffraction conditions were localized by signals measured by the detector (Fig. 2*a*). After defining the two-dimensional real-space coordinates (x, y) (Fig. 2*b*) and the ROIs within the detector area [indicated with squares in Fig. 2(*a*)], maps were recorded for each ω (Fig. 2*c*) leading to a three-dimensional reciprocal-space map. The incidence angles were chosen to be in the vicinity of the probed *hkl* reflections. A more detailed description of the experimental routine and data treatment can be found in the literature (Chahine *et al.*, 2014, 2015).

A complete five-dimensional data set was acquired on a $CuInSe_2$ thin film, sampling with a step size of 100 nm in the two-dimensional real-space scan. Given Q, the interplanar distance d and the tilt angle φ can be calculated according to

$$d = 2\pi/|Q| = 2\pi/\left(|Q_x^2 + Q_y^2 + Q_z^2|^{1/2}\right) \quad (1)$$

and

$$\varphi = (180^\circ/\pi)\arccos\left(|Q_z|/|Q|\right). \quad (2)$$

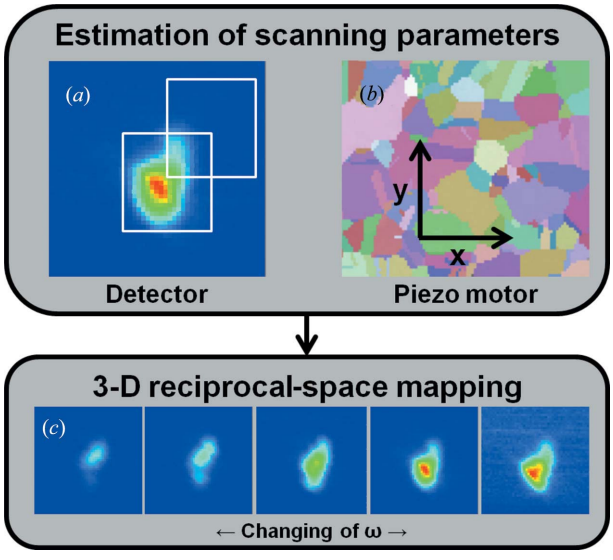

Figure 2
Schematic drawing of the experimental approach. After the estimation of the scanning parameters concerning the real-space (*b*) and the detector regions (*a*), maps (x, y) for each chosen incidence angle ω in the vicinity of the *hkl* reflection were recorded (*c*).

The investigated $CuInSe_2$ thin film did not exhibit a strong preferred orientation, which leads to the assumption of adjacent $CuInSe_2$ grains with predominantly large misorientations. Therefore, atomic planes are unlikely to cross grain boundaries, and as a result, by choosing appropriate diffraction conditions, a single *hkl* reflection within an individual $CuInSe_2$ grain can be resolved, provided the photon intensity is sufficient. Fig. 3(*a*) shows the integral intensity measured for the 155_{cubic} reflection. Areas with higher intensities were taken into account for strain and tilt evaluation within one single grain as their sizes are concurrent with the actual grain sizes of about 1–2 µm in diameter. To distinguish tilt distributions within the 155_{cubic} plane, deviations from the coplanar geometry or the normal orientation of the plane have to be measured. Using equation (2), tilt deviations were calculated and plotted for areas of interest in the real space (see Fig. 3*b*). Low tilt deviations of the order of $10^{-3\circ}$ were found to be

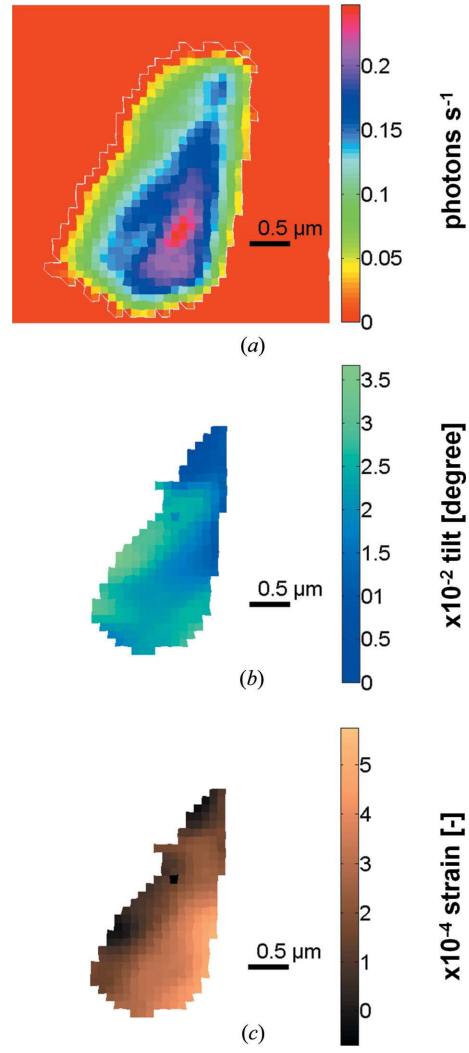

Figure 3
(*a*) Measured integral intensity of the 155_{cubic} reflection, showing the shape of a $CuInSe_2$ grain. (*b*) Calculated tilt-distribution map (orientational variance) of the measured grain. (*c*) Strain distribution map based on evaluated d_0 location. The data were acquired at an X-ray energy of 8.9 keV, a beam size of 100 × 100 nm and a step size in the scan of 100 nm.

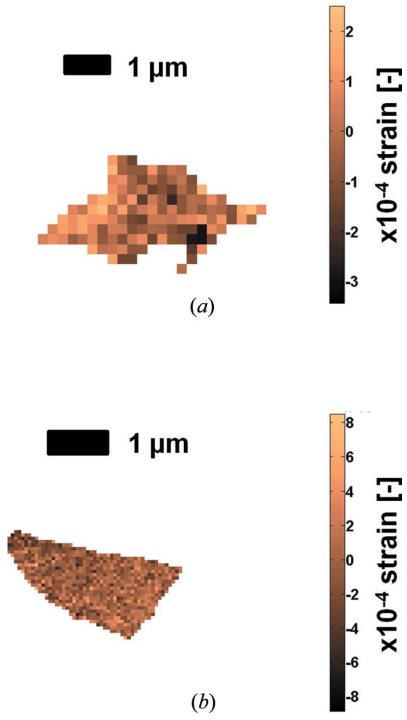

Figure 4
Out-of-plane microstrain distribution maps from (*a*) Raman microspectroscopy and (*b*) high-resolution EBSD measurements, conducted on $CuInSe_2$ thin films from the same deposition run as the one shown in Fig. 2.

present within the investigated plane. In order to obtain relative microstrain changes within individual $CuInSe_2$ grains, it is a prerequisite to determine the positions of unstrained states in these grains. The lowest tilt deviation was assumed to be a good choice for an unstrained position within the grain, although tilt within the plane does not necessarily induce strain. Positions near the intensity maximum, *i.e.* in the diffraction condition, might also be a good position to be regarded as unstrained. By calculating the out-of-plane strain

$$\varepsilon = (d - d_0)/d_0, \tag{3}$$

where d_0 is the unstrained interplanar distance, a microstrain distribution within a single grain is obtained, with values mostly of the order of 10^{-4} (Fig. 3*c*).

The results shown in Fig. 3 were reproduced by measuring tilt and strain distributions for a second grain using the 336 reflection. The integral intensity was lower, mainly because of the different diffraction conditions. The second grain also exhibited strain distributions with values of about 10^{-4}.

Fig. 4 shows microstrain distributions acquired by Raman microspectroscopy (Fig. 4*a*) and high-resolution EBSD (Fig. 4*b*). Both microstrain distributions in Fig. 4 exhibit values of the same order of magnitude as the microstrain values in Fig. 3(*c*).

µ-HRXRD measurements of $CuInSe_2$ thin films allow the estimation of microstrain and tilt distribution within individual grains at the submicrometre scale. Microstrain values of about 10^{-4} were determined within polycrystalline layers which were buried in complete solar-cell stacks. Since µ-HRXRD is directly assessing lattice displacements, the obtained microstrain distributions acquired by means of high-resolution EBSD (Wilkinson, 1996; Wilkinson *et al.*, 2006) and Raman microspectroscopy (Schmid *et al.*, 2015) measurements can be supported.

Acknowledgements

Financial support by the Helmholtz Virtual Institute 'Microstructure Control in Thin-Film Solar Cells', VH-VI-520, is gratefully acknowledged.

References

Becker, M., Scheel, H., Christiansen, S. & Strunk, H. P. (2007). *J. Appl. Phys.* **101**, 063531.
Berger, L. I. (1996). *Semiconductor Materials*. Boca Raton: CRC Press.
Caballero, R., Kaufmann, C. A., Efimova, V., Rissom, T., Hoffmann, V. & Schock, H.-W. (2013). *Prog. Photovolt. Res. Appl.* **19**, 547–551.
Chahine, G. A., Richard, M.-I., Homs-Regojo, R. A., Tran-Caliste, T. N., Carbone, D., Jacques, V. L. R., Grifone, R., Boesecke, P., Katzer, J., Costina, I., Djazouli, H., Schroeder, T. & Schülli, T. U. (2014). *J. Appl. Cryst.* **47**, 762–769.
Chahine, G. A., Zoellner, M. H., Richard, M.-I., Guha, S., Reich, C., Zaumseil, G., Capellini, G., Schroeder, T. & Schülli, T. U. (2015). *Appl. Phys. Lett.* **106**, 071902.
Dingley, D. J., Wilkinson, A. J., Meaden, G. & Karamched, P. S. (2010). *J. Electron Microsc.* **59**, S155–S163.
González, J., Quintero, M. & Rincón, C. (1992). *Phys. Rev. B*, **45**, 7022–7025.
Kaufmann, C. A., Neisser, A., Klenk, R. & Scheer, R. (2005). *Thin Solid Films*, **480–481**, 515–519.
Kriegner, D., Wintersberger, E. & Stangl, J. (2013). *J. Appl. Cryst.* **46**, 1162–1170.
Schmid, T., Schäfer, N., Levcenko, S., Rissom, T. & Abou-Ras, D. (2015). *Sci. Rep.* **5**, 18410.
Sun, Y., Thompson, S. E. & Nishida, T. (2007). *J. Appl. Phys.* **101**, 104503.
Theodoropoulou, S., Papadimitriou, D., Anestou, K., Cobet, C. & Esser, N. (2009). *Semicond. Sci. Technol.* **24**, 015014.
Wilkinson, A. J. (1996). *Ultramicroscopy*, **62**, 237–247.
Wilkinson, A. J., Meaden, G. & Dingley, D. J. (2006). *Ultramicroscopy*, **106**, 307–313.